Geochimica et Cosmochimica Acta 408 (2025) 132–143

Contents lists available at ScienceDirect

Geochimica et Cosmochimica Acta

journal homepage: www.elsevier.com/locate/gca

Phosphate effects on rare earth element sorption onto kaolinite: molecular-scale insights at circumneutral pH

Hang Xu [a], Johannes Leisen [b], Alicia S. Robang [c], Yinghao Wen [a], Biao Wan [d], Simin Zhao [a], Anant Paravastu [c], Brian L. Phillips [e], Yuanzhi Tang [a,*]

[a] School of Earth and Atmospheric Sciences, Georgia Institute of Technology, 311 Ferst Dr, Atlanta, GA 30332, United States
[b] School of Chemistry and Biochemistry, Georgia Institute of Technology, 311 Ferst Dr, Atlanta, GA 30332, United States
[c] School of Chemical and Biomolecular Engineering, Georgia Institute of Technology, Atlanta, GA 30332, United States
[d] Environmental Protection Key Laboratory of Soil Health and Green Remediation, College of Resources and Environment, Huazhong Agricultural University, Wuhan 430070, China
[e] Department of Geosciences, Stony Brook University, Stony Brook, NY 11794, United States

ARTICLE INFO

Associate editor: Juan Liu

Keywords:
Rare earth elements (REEs)
Phosphate
Kaolinite
REE transport
Surface complexation
Molecular interaction
Nuclear magnetic resonance (NMR) spectroscopy

ABSTRACT

Rare earth elements (REEs) are critical minerals that are indispensable for the clean energy transition. Understanding their occurrence and behavior in highly weathered environments provides valuable insights into the identification and prediction of potential REE resources. Phosphate (P) plays an important role in controlling the geochemical behaviors of REE during weathering and secondary deposition. REE-phosphate minerals, such as monazite and xenotime, are among the important natural sources of REE. However, the molecular-scale reaction mechanisms underlying phosphate-REE interactions in weathering environments remain unclear. This study investigates the interaction between phosphate and yttrium on the surface of kaolinite, a representative and abundant clay mineral in highly weathered environments. At circumneutral pH 6, phosphate inhibits yttrium mobilization by forming ternary kaolinite-yttrium-phosphate complexes and surface precipitation. The reaction mechanisms identified in this study are distinct from previously reported adsorption-dominated processes on clay minerals that govern REE immobilization during chemical weathering. Solid-state nuclear magnetic resonance (NMR) spectroscopy, including ^{31}P direct polarization magic angle spinning (DP/MAS) and $^{1}H - ^{31}P$ cross polarization (CP) rotational echo adiabatic passage double resonance (REAPDOR) analyses, provides direct molecular-scale evidence for the yttrium-phosphate surface complexation on kaolinite. Quantification of atomic distances by numerical simulations further substantiates the formation of ternary surface complexes. These mechanistic findings enhance our understanding of phosphate-mediated REE mobilization, transport, and redeposition in natural environments.

1. Introduction

Rare earth elements (REEs), including the lanthanides, yttrium (Y), and scandium (Sc), are the “essential vitamins” of many modern technologies, such as electric vehicles, wind turbines, permanent magnets, and energy-efficient lighting (Feng et al., 2021; Goodenough et al., 2018; Ormerod et al., 2023; Zhang et al., 2021; Zhou et al., 2022). As the global transition to renewable energy accelerates, the demand for REE continues to grow. However, the uneven global distribution of REE natural resources and the supply–demand deficit have put the REE industry in a challenging position. Addressing current challenges requires the exploration of new REE resources and design of sustainable extraction technologies, both anchoring on a comprehensive understanding of the fundamental processes governing REE occurrence and mobilization in natural systems.

Economically significant REE deposits commonly develop in highly weathered regolith under warm and humid climatic conditions. Prolonged weathering mobilizes REE from parent rocks and drives their redistribution and fractionation, while simultaneously converting feldspar and mica in granite bedrocks to clay minerals. The resulting kaolinite-halloysite assemblages are ubiquitously associated with REE accumulation and play an important role in controlling REE mobility. In

* Corresponding author.
E-mail address: yuanzhi.tang@eas.gatech.edu (Y. Tang).

https://doi.org/10.1016/j.gca.2025.09.040
Received 20 April 2025; Accepted 26 September 2025
Available online 29 September 2025

particular, their high surface areas and reactive aluminol or silanol groups at defect sites or broken edges provide efficient substrates for REE adsorption and retention (Borst et al., 2020; Li and Zhou, 2020; Liu et al., 2022; Schoonheydt and Johnston, 2013; Wang et al., 2023a; Yang et al., 2019). Ion adsorption deposits (IADs) exemplify such regolith-hosted type and constitute the principal commercial sources of heavy rare earth elements (HREE) located in Southeastern China, Madagascar, Brazil, and Thailand (Giovannini et al., 2017; Janots et al., 2015; Li et al., 2019; Sanematsu and Watanabe, 2016). A typical regolith-hosted IAD profile comprises four distinct horizons: bedrock, semi-weathered zone, saprolite, and highly leached topsoil. Within the topsoil, REE complexes with various natural ligands are transported by groundwater and rainfall, migrating downward into the saprolite where they accumulate via sorption onto clay minerals (Costa et al., 2020; Xu et al., 2017). Kaolinite dominates the clay fraction in this REE-accumulation horizon, particularly in Chinese IADs which supply ~ 80 % of global HREE production. To investigate the underlying molecular-scale mechanism of REE retention on kaolinite, Borst et al. (2020) used X-ray absorption spectroscopy (XAS) to characterize IAD samples from China and Madagascar. They showed that Y and neodymium (Nd) primarily form eight- to nine- coordinated outer-sphere complexes on kaolinite surfaces (Borst et al., 2020). More recently, element-specific surface crystallography has revealed the complexity of REE adsorption mechanisms, indicating discorded coordination with mixed inner- and outer- sphere complexes on aluminum-rich clays (Fang et al., 2025). However, characterizing the local coordination environment of REE by XAS remains challenging, especially in REE-clay systems. For example, a recent study on REE sorption on kaolinite discussed the uncertainties in shell-by-shell fitting of extended X-ray absorption fine structure (EXAFS) data, due to the damping of oscillations beyond $k \approx 9$ Å^{-1}, large first-shell disorder, weak backscattering from light second-shell atoms (Al, Si) at the ytterbium (Yb) L_3-edge, and overlapping Yb–Al/Si distances (Ramazanova et al., 2025). To address the disordered coordination environment of REE, Fang et al. employed high-resolution X-ray reflectivity (XR) and resonant anomalous XR (RAXR) to investigate REE sorption on alumina (001) and (012) single-crystal surfaces (Fang et al., 2025). XR and RAXR can provide both total and element-specific interfacial structures for a single solid surface, yet the authors note that these methods require large atomically flat single crystals (>1 mm), which are not unavailable for kaolinite or related clay minerals nor representative of their occurrence in natural settings (Fang et al., 2025). These recent studies using advanced methods highlight the necessity of a multi-method approach to obtain a comprehensive mechanistic understanding of REE sorption and weathering behaviors at molecular scale.

While IADs have been one key system for REE research from field-scale studies to molecular-level adsorption mechanisms and remain the cornerstone of global supply, recent field work has uncovered significant REE enrichment in Georgia kaolin district and alluvial sediments across Atlantic Coastal Plains in the Southeast U.S. Field studies have reported REE concentrations (140 – 6,500 ppm) in these sedimentary systems comparable to those of IADs in South China, which underscores the resource potential of these regions (Bern et al., 2016; Boxleiter and Elliott, 2023). Formed under broadly similar subtropical climatic conditions to the abovementioned regolith-hosted IADs, the southeastern U.S. alluvial sedimentary deposits also experienced deep weathering. Saprolitization and diagenetic alteration, serving as the primary chemical weathering processes, yield kaolin-rich materials that supply the sedimentary deposits and result in REE leaching and subsequent redistribution, as well as the concomitant deposition of authigenic kaolinite (Cheshire et al., 2018). However, a key difference from traditional IADs lies in REE occurrences. Unlike IAD saprolites, these sediments show a strongly positive phosphate-REE correlation (Bern et al., 2016). Petrographic evidence and micro-spectroscopic studies reveal that REE-phosphate minerals are the most significant and stable natural REE reservoirs in these sediments, far outweighing other REE-bearing phases and occurring in close spatial association with the kaolinite matrix (Bern et al., 2016; Boxleiter and Elliott, 2023). For instance, X-ray fluorescence mapping shows a strong co-localization of Nd^{3+} and PO_4^{3-} on the surfaces of kaolinite particles (Cheshire et al., 2018); additionally, the precipitation of secondary phosphates such as florencite ($CeAl_3(PO_4)_2(OH)_6$) has been identified within the clay assemblage in natural samples (Cheshire et al., 2018). These findings imply phosphate (P) as a key driver in REE sequestration in certain natural systems. Two non-exclusive hypotheses can explain the prevalence of REE in such forms, i) higher inherited P_2O_5 content supplies ample phosphate during secondary weathering; ii) sorption of dissolved REE and phosphate from easily weathered detrital phases would interact with clay mineral surfaces, eventually form the secondary phosphate minerals (Elliott et al., 2018). Critically, both scenarios hinge on a sequence of molecule-scale interactions among REE, phosphate, and clay mineral surfaces, which however remains poorly understood. Additionally, previous studies have revealed that secondary weathering can heavily influence REE signatures, resulting in REE remobilization and redistribution onto clay minerals. However, the mechanistic pathways governing REE-P interactions at clay mineral surfaces are currently lacking, which also highlights the need for further investigations.

Various biogeochemical processes affect the REE transport and occurrence during secondary weathering in natural environments, such as ion sorption, ligand complexation, dissolution, precipitation, and redox-driven remobilization (Borst et al., 2020; Elliott, 2020; Emsbo et al., 2015; Huang et al., 2021a; Li and Zhou, 2020; Stolpe et al., 2013; Xu et al., 2022). For both aforementioned representative types of natural REE reserves, natural ligands play an important role in controlling REE behaviors. For example, Cl^-, F^-, SO_4^{2-}, CO_3^{2-}, and PO_4^{3-} derived from parent accessory minerals such as fluorite (CaF_2), calcite ($CaCO_3$), and apatite ($Ca_{10}(PO_4)_6(OH,F,Cl)_2$) exhibit varying complexation constants with REE (Aubert et al., 2001; Byrne et al., 1996; Jonasson et al., 1985; Louvel et al., 2022). These ligands influence the mobility and fractionation of REE that are released from primary REE-bearing minerals (e.g., Bastnäsite (Ce,La)(CO_3)F), apatite ($Ca_{10}(PO_4)_6(OH,F,Cl)_2$), etc.), as well as the solubility of REE minerals (Cheshire et al., 2018; Kanazawa and Kamitani, 2006; Lee and Byrne, 1993; Tang and Johannesson, 2010; Turner, 2015). Among these ligands, phosphate is particularly important due to its strong complexation with REE and its ubiquitous occurrence in natural systems (Liu and Byrne, 1997). Specifically, naturally labile phosphate derives from the dissolution of minerals with relatively low weathering resistance, for instance apatite, rhabdophane, and florencite-(Ce), as well as from biogenic inputs such as the decomposition of organic debris (Föllmi, 1996; Fu et al., 2024). Indeed, REE phosphate minerals, xenotime, monazite, and apatite, account for a large share of the REE budget in many highly-weathered deposits worldwide (Dushyantha et al., 2020). Yet laboratory studies have not fully elucidated the water–mineral interfacial reactions that mediate REE-P coupling mechanisms during chemical weathering, which are likely to initiate the formation of secondary REE-phosphate minerals within clay assemblages. Addressing this knowledge gap is necessary to advance our understanding of REE immobilization, mobilization, and transport, and will inform strategies for exploration and identification of REE resources, as well as the design of more efficient extraction and recovery processes.

This study aims to explore the important roles of phosphate in the mobility and distribution of REE on clay minerals under environmentally relevant conditions. Y was selected as a probe for REE. Additionally, since these REE resources are found in highly weathered rocks containing kaolin, e.g. regolith-hosted or lateritic deposits, including mined kaolin deposits, kaolinite was chosen as the mineral substrate because of its chemical stability, prevalence in highly weathered REE deposits, and capacity for both ions exchange and surface adsorption (Borst et al., 2020; Huang et al., 2021b; Li et al., 2019; Wu et al., 2023). Batch sorption experiments were conducted by adding dissolved Y and P to kaolinite suspension in different sequences. These sequential-sorption batches reproduced the staggered release of REE and P from natural

labile sources, and the attendant interfacial interactions during secondary chemical weathering. Interfacial reaction mechanisms were characterized using advanced spectroscopy techniques. Considering the sensitivity limitations of X-ray absorption spectroscopy (XAS) in detecting subtle changes in REE local bonding environments in REE-clay mineral system (Fang et al., 2025; Ramazanova et al., 2025), advanced solid-state nuclear magnetic (NMR) spectroscopy techniques were employed as a complimentary approach. Specifically, one dimension (1D) ^{31}P nuclear magnetic resonance (^{31}P NMR) and ^{31}P/^{27}Al Rotational Echo Adiabatic Passage Double Resonance (REAPDOR) NMR experiments were performed to characterize phosphate speciation and coordination, elucidate bonding environments, and determine the interfacial structures of surface complexes. 1D ^{31}P solid-state NMR is a powerful technique to characterize the sorption behaviors of phosphate on aluminum (hydro)oxide minerals (Bleam et al., 1989; Li et al., 2013a; Li et al., 2013b). REAPDOR leverages the high sensitivity of ^{31}P nuclei to provide precise structural information on ^{27}Al–^{31}P proximity, which enables the inference of the coordination and interfacial structure of Y-associated phosphate to kaolinite Al-octahedral layer. Numerical simulations of REAPDOR data were applied to quantify the atomic distances between kaolinite surface and the Y-P complexes. Our findings elucidate the interfacial reactions between Y and P on the kaolinite surface (e.g., surface complexation and precipitation) and provide molecular-level insights into the influences of phosphate on REE occurrences in complex natural matrix.

2. Materials and methods

2.1. Materials

Kaolinite KGa-1b, with a surface area of 10.05 ± 0.02 m^2 /g and cation exchange capacity (CEC) of 2.0 meq/100 g, was purchased from the Clay Minerals Society. Yttrium(III) chloride hexahydrate ($YCl_3 \cdot 6H_2O$, 99.9 % purity), indium internal standard (TraceCERT), and REE mix standard (TraceCERT) were purchased from Millipore Sigma (Burlington, USA). Potassium dihydrogen phosphate (KH_2PO_4, ACS grade) was obtained from Strem Chemicals (Newburyport, USA). Sodium hydroxide (NaOH) and hydrochloric acid (HCl) were purchased from Sigma-Aldrich (St. Louis, USA). All solutions were prepared using ultrapure deionized (DI) water (18.2 MΩ·cm) from a Barnstead Nanopure system (Thermo Fisher Scientific, Waltham, USA).

2.2. Batch sorption experiments

Control experiments were conducted to determine the sorption pH edges and isotherms for Y or P alone on kaolinite. The pH edge experiments were conducted at pH 1–9 with a fixed concentration of 50 μM for Y or P (**Text S1**). Based on Y and P sorption behaviors as a function of pH, subsequent sorption isotherm experiments were conducted at varied Y or P concentrations at pH 6 (**Text S2**). This pH also falls within the typical range of REE-enrichment horizons in highly-weathered deposits, reflecting natural conditions (Wang et al., 2023b).

Based on the results of pH edge and isotherm experiments, three sets of sequential sorption experiments and corresponding controls were conducted to simulate potential interactions of Y and P on kaolinite surfaces. The experimental conditions were summarized in Table 1. Kaolinite suspensions (30 mL, 1 g/L) were prepared in glass flasks, sonicated for an hour, and equilibrated overnight under magnetic stirring at room temperature at pH 6.

For Experimental Set I (Seq-500Y-100P), II (Seq-500Y-500P), and III (Seq-500Y-1000P), the reaction steps were as follows. In Step 1 (Y sorption): Y^{3+} stock solution was added to the kaolinite suspensions to achieve 500 μM of Y^{3+} and allowed to react for 24 h. Throughout the pre-equilibrium and sorption processes, solution pH was maintained at pH 6 by manual titration using 0.1 M HCl and 0.1 M NaOH. In Step 2 (P sorption), the suspension was centrifuged at 10,000 rpm for 15 min.

Table 1
Experimental sets, corresponding labels, and sorption sequences of yttrium and phosphate in batch sequential sorption experiments and controls. (Note: Set I – IV are sequential sorption; Control I – IV are corresponding controls).

Experimental sets	Sample label	Addition sequence	
		Step 1 (24 h)	Step 2 (24 h)
Set I (sequential sorption)	500Y100P	500 μM Y	100 μM P
Control I (P sorption)	100P	–	100 μM P
Set II (sequential sorption)	500Y500P	500 μM Y	500 μM P
Control II (P sorption)	500P	–	500 μM P
Set III (sequential sorption)	500Y1000P	500 μM Y	1000 μM P
Control III (P sorption)	1000P	–	1000 μM P
Set IV (sequential sorption)	500P500Y	500 μM P	500 μM Y
Control IV (Y sorption)	500Y	–	500 μM Y

After decanting the supernatant, the wet paste was washed with DI water, resuspended in 30 mL of DI water, and sonicated for 30 min. Analysis of Y concentration in the washing solutions indicated that > 95 % of the sorbed Y remained on kaolinite surfaces after washing (**Fig. S1**). After the resuspension, phosphate stock solution was added to achieve 100 μM, 500 μM, and 1 mM for experimental Set I, II, and III respectively. Control experiments I–III were conducted with the same initial P concentrations and kaolinite loadings without Y. All reactions were conducted for 24 h at pH 6. The pH throughout all the batch sorption experiments was at 6.0 ± 0.2 by adjustment with HCl and NaOH. Aliquots (3 mL) of the reaction suspension were filtered (0.22 μm) and analyzed for P concentration.

For the Experiment Set IV (Seq-500P-500Y), kaolinite suspensions were prepared as previously described. In Step 1 (P sorption), phosphate stock solution was first added to achieve 500 μM and allowed to react at pH 6 for 24 h, followed by centrifugation and DI rinsing as described above. Around 90 % of the adsorbed P remained after the washing process (**Fig. S1**). In Step 2 (Y sorption), Y was added to the resuspended P-loaded kaolinite to achieve 500 μM Y. Control experiment IV consisted of 500 μM Y sorption without P. Aliquots of samples were collected, filtered, and analyzed for dissolved Y concentration using inductively coupled plasma – mass spectroscopy (ICP-MS) (**Text S3**). Solid samples from all experimental sets were harvested by filtration through 0.22-μm membranes and freeze-dried for further solid characterization.

2.3. Solid and liquid phase characterizations

The concentration of dissolved Y was analyzed using ICP-MS (**Text S3**). The concentration of P was determined using the phosphomolybdate colorimetric assay on an Agilent Carey 60 ultraviolet–visible (UV – vis) spectrometer (Santa Clara, USA) (Murphy and Riley, 1962). Aqueous speciation and supersaturation of the system were modeled by thermodynamic calculation using the program PHREEQC version 3 (Parkhurst and Appelo, 2013) and MINTEQ 4.0 (**Text S4**).

For solid-phase analysis, freeze-dried solid samples were characterized using 1D ^{31}P DP/MAS solid state nuclear magnetic resonance on a Bruker AVIII-HD 300 two-channel NMR spectrometer at a ^{1}H frequency of 300 MHz (Rheinstetten, Germany) (**Text S5**). To investigate interatomic distances and local coordination environments among Y, P, and the kaolinite surfaces, ^{1}H→^{31}P/^{27}Al CP-REAPDOR solid-state NMR spectra were obtained using a Bruker AVIII 400 three-channel NMR spectrometer equipped with a MAS triple-resonance probe operating with a single coil tuned to ^{27}Al, ^{31}P, and ^{1}H (**Text S6**). Specifically, the 400 MHz Bruker AV3 spectrometer (9.4 T) with a three-channel MAS probe allowed tuning to ^{1}H, ^{31}P, and ^{27}Al. The probe uses 4 mm diameter zirconia rotors which were spun at 10 kHz. The relaxation delay was 5 s. For REAPDOR NMR experiments, the ^{31}P 180° pulse length was 10 μs, and ^{27}Al pulse in the middle of the dephasing pulse train had a duration and strength equal to 1/5 of the rotor period and 75 kHz, respectively. A scan number of 1024 was carried out for data acquisition of each spectrum. The dipolar dephasing sequence (*S*) and second

control spectrum (S_0) were measured as a function of 8 different dephasing times, and the difference ($\Delta S = S_0 - S$) in peak intensity between S and S_0 at the same dephasing sequence length (τ) was calculated. Numerical simulation of the REAPDOR dephasing curves was performed using the NMR SPINEVOLUTION simulation package (**Text S6**) (Veshtort and Griffin, 2006) to estimate interatomic distances.

Y K-edge X-ray absorption spectroscopy (XAS) was conducted on the reacted solids after sorption experiments at Beamline 5-BM-D at the Advanced Photon Source (APS), Argonne National Laboratory, Lemont, IL, USA. The dried solids were loaded onto epoxy Kapton tape before XAS measurements. All spectra were collected in both transmission and fluorescence modes. A Y foil was measured simultaneously in transmission for energy calibration (at 17,038 eV). Multiple scans (4–6) were collected for each sample, averaged, and normalized. Morphological and elemental analysis of the reacted solids were conducted using high resolution transmission electron microscopy (HRTEM) (Hitachi HD2700 HRTEM-EDS; Tokyo, Japan), operated at an accelerating voltage of 200 kV combined with energy dispersive spectroscopy (EDS) (Ding et al., 2018). Powder samples were ultrasonically dispersed in ethanol, and 10 μL aliquots were dropped onto carbon-coated copper grids and air-dried prior to imaging. Elemental distribution maps for Y and P in selected regions of interest were obtained from EDS mode, providing spatial information on the elemental composition.

3. Results

3.1. Sorption behaviors of yttrium and phosphate on kaolinite

Preliminary experiments were performed to evaluate the sorption behaviors of Y or P alone on kaolinite (**Text S1 — S2**), which has a point of zero charge (PZC) of 4–4.5 (Ganor et al., 2003; Li et al., 2010; Schroth and Sposito, 1997; Yang and Steefel, 2008). The pH edge results showed an increased Y uptake with increasing pH (Fig. 1), which can be attributed to the surface deprotonation of kaolinite and subsequent enhanced electrostatic attraction between Y^{3+} and kaolinite under alkaline conditions. Sorption of P, however, increased from pH 2 to a peak at pH 4 and then decreased as pH increases to 10 (Fig. 1). Based on PHREEQC thermodynamic modeling, P mainly exist as H_3PO_4 and $H_2PO_4^-$ at pH 2–4 and $H_2PO_4^-$ and HPO_4^{2-} at pH 4–10 (Figs. 2a and 2b). From pH 4 to 2, the electrostatic attraction between positively charged kaolinite surface and P decreased as the fraction of neutral H_3PO_4 increases. From pH 4 to 10, the changes in P speciation and surface charge of kaolinite resulted in electrostatic repulsion.

Despite their different pH-dependent sorption behaviors, the comparable distribution coefficients (K_d) of Y and P at pH 6 suggested comparable sorption capacities on kaolinite surfaces (Fig. 1). This observation led to our hypothesis that competitive sorption and ion-specific interactions dominate at pH 6 rather than other pH conditions (Fig. 1). Y sorption isotherms at pH 6 showed a positive correlation between sorbed Y and its initial concentration (**Fig. S2**), with maximum sorption capacity reached at initial concentrations of 100 μM or higher. For P, an uptake plateau was achieved at concentrations of 50 μM or above (**Fig. S3**). Based on these isotherms, 500 and/or 1000 μM of Y and P concentrations were selected for batch sequential sorption

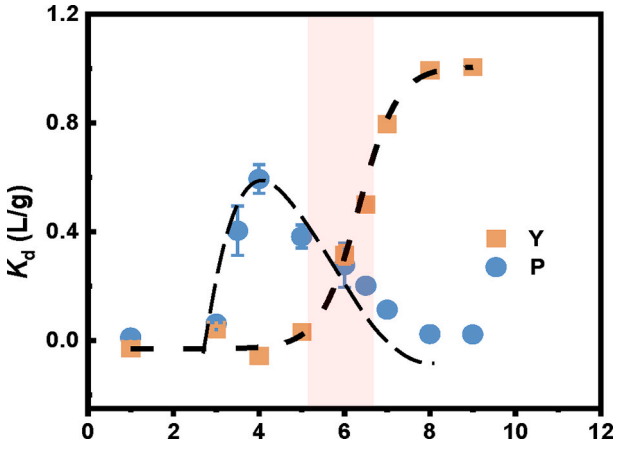

Fig. 1. The distribution coefficient (K_d = V(C_0-C_{eq}) /mC_{eq}, C_0: initial concentration; C_t: the species concentration at sorption equilibrium; V: volume of kaolinite suspension; m: mass of kaolinite) with 50 μM initial concentration of dissolved Y and P at pH 1–9.

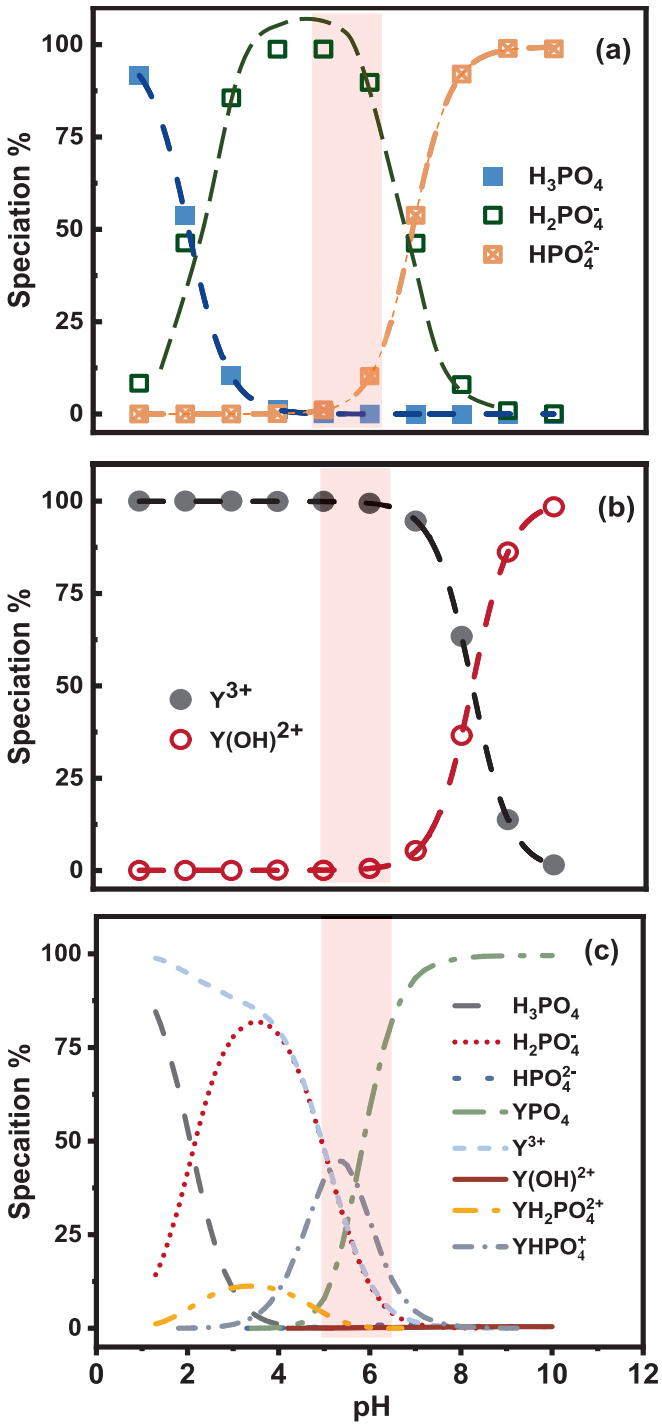

Fig. 2. PHREEQC speciation calculation at pH range 1–10 for **(a)** 500 μM dissolved phosphate only, **(b)** 500 μM dissolved yttrium, and **(c)** the co-occurrence of 500 μM yttrium and 500 μM phosphate.

experiments to ensure the system reaching maximum uptake.

Sequential sorption experiments were conducted to simulate different sequences of Y and P occurrences during weathering processes (Table 1). In the first sequence, Y was allowed to interact with kaolinite for 24 h before P was introduced. With 100 μM of P (Set I, 500Y100P), sorption of P onto Y-treated kaolinite (30.09 %) was enhanced compared to Y-untreated kaolinite (21.06 %, Control I) (Fig. 3a). Such difference suggests that the adsorbed Y interacts with dissolved P and facilitates P sorption onto kaolinite. To examine whether a higher P concentration would affect the mobilization of adsorbed Y, sorption of P at initial concentrations of 500 μM and 1 mM were performed which however showed similar trend (10.68 % for Set II vs. 8.23 % for Control II, 7.64 % for Set III vs. 4.02 % for Control III) (Fig. 3a). On the other hand, sequential sorption with the opposite order was also conducted, where P first interacted with kaolinite, followed by Y addition. Y uptake by P-treated kaolinite was 12.48 % (Set IV), whereas that by pristine kaolinite (without P pre-treatment) was only 2.73 % (Control IV) (Fig. 3b). The differences in the uptake of Y and P between sequential sorption and control groups support our hypothesis that interfacial interactions between Y and P on the kaolinite surfaces might influence Y redistribution and the formation of secondary Y-phosphate minerals.

3.2. Y speciation characterization by EXAFS analysis

To characterize Y coordination environments, Y K-edge XANES spectra for the sequential-sorption samples and reference compounds are shown in Fig. 4. All the spectra exhibited a major Y peak at 17054 eV. Additionally, the Y-P co-precipitation and co-sorption references displayed a small shoulder at 17062 eV, whereas no apparent shoulder is observed in Y sorption-only reference (500Y). This suggests that the presence of Y-P associated bonding can potentially produce the shoulder near 17063 eV, and may serve as a probe of Y local bonding to differentiate Y speciation between Y local bonding with and without proximal P. The spectra of the sequential-sorption samples also showed the major peak and small shoulder at ~ 17062 eV, which is plausible evidence for similar local bonding environments to the co-precipitation and co-sorption references rather than the Y sorption-only reference. Nevertheless, we note that EXAFS analysis is required for detailed information on Y coordination. To this end, we conducted EXAFS analysis, and the k^2-weighted Y K-edge EXAFS data are shown in **Fig. S4**. Unfortunately, the damped *k*-space oscillations and limited data quality render the corresponding Fourier transform inconclusive, a complementary technique is therefore needed for robust characterization of surface structures.

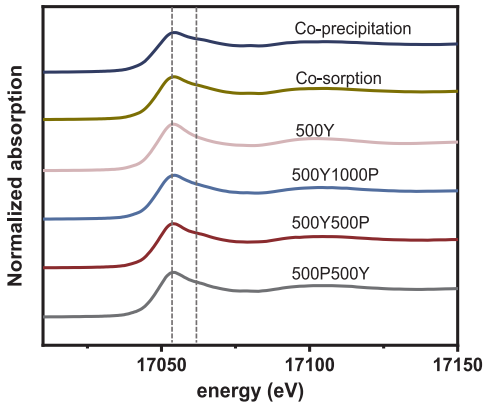

Fig. 4. Normalized Y XANES spectra of sequential sorption samples and references. Sample co-precipitation: 10 mM yttrium and phosphate bulk precipitation; co-sorption: 500 μM yttrium and phosphate co-sorption with kaolinite; 500Y: 500 μM yttrium sorption only.

3.3. Phosphate speciation characterization by 1D ^{31}P NMR

Since the Y XENES and EXFAS provided limited information on surface structures, we sought local bonding information from the phosphate perspective. To elucidate the molecular-level reaction mechanisms between Y and phosphate on kaolinite surface, the reacted solids were characterized using solid-state NMR. ^{31}P solid-state NMR is an effective method for investigating P sorption behaviors on aluminum (hydro)oxide mineral (Bleam et al., 1989; Li et al., 2013a; Li et al., 2013b). In this study, the ^{31}P DP/MAS NMR spectra of kaolinite samples were measured to determine adsorbed P speciation. The spectrum for 500P (Control I) showed a single peak centered at a chemical shift (δ_p) of −10 ppm (Fig. 5a), indicating a single phosphate species sorbed on the kaolinite surface. Chemical shifts in the 0 to −10 ppm range have been previously attributed to inner-sphere complexes between P and aluminum (hydro)oxide mineral surfaces due to changes in electron density around ^{31}P nuclei and the resulting shielding effects of Al − O − P linkages (Li et al., 2013a). Specific examples of such complexes include δ_p at −11 ppm for wavellite, −10.2 ppm for brazilianite, −6 ppm for phosphate sorbed by boehmite and amorphous aluminum hydroxide, −4.5 ppm for gibbsite, −3 ppm for γ-alumina (Cade-Menun, 2005; Li et al., 2013a; Yan et al., 2015). Consistent with prior studies, δ_p at −10 ppm in the NMR spectrum of sample 500P (Control I) is assigned to the inner-sphere complexation between P and kaolinite.

In contrast, the NMR spectra of sequential sorption samples displayed multiple peaks, indicating the presence of different P species (Figs. 5b - 5d). Each spectrum showed dominant peaks at $\delta_p = -4$ ppm

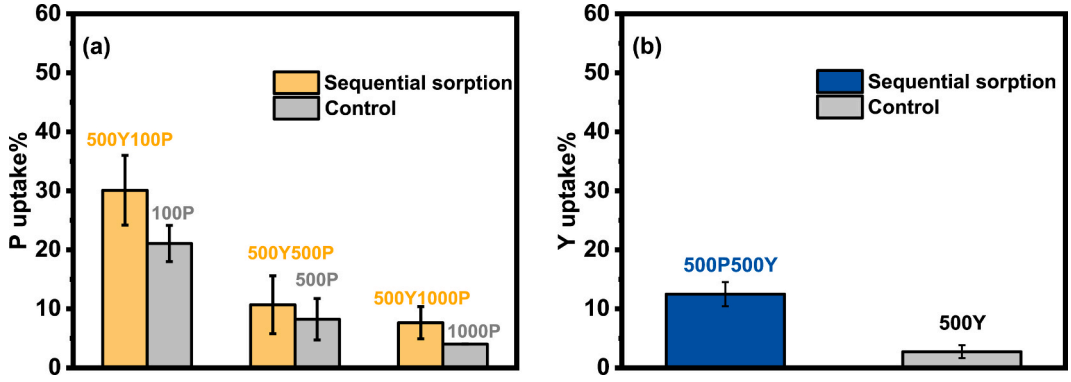

Fig. 3. **(a)** Phosphate uptake of sequential sorption and **(b)** yttrium uptake of sequential sorption. (The yellow and blue bars refer to sequential sorption experimental sets, and gray bars represent control experimental sets). Note: sequential sorption involves introducing either yttrium or phosphate into kaolinite suspension first, followed by the addition of the other one; control involves adding only yttrium or phosphate into kaolinite suspension.

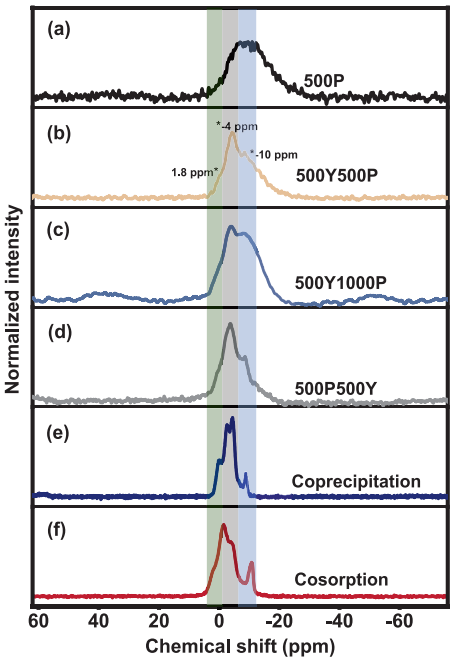

Fig. 5. **(a)** Phosphate sorption alone, **(b–d)** 1D ^{31}P solid-state NMR spectra for sequential sorption, **(e)** 10 mM Y and P coprecipitation (no kaolinite), and **(f)** cosorption (with kaolinite). Green, gray, and blue vertical shadings represent chemical shift at 1.8, −4, and −10 ppm, respectively.

and −10 ppm and a shoulder at $\delta_p = 1.8$ ppm. All peaks were well-fitted with the Gaussian curves (**Fig. S5**, **Table S1**), though variations in the peak width and chemical shift were noted, likely due to slight differences in the amounts of sorbed phosphate, phosphate precipitates, and ternary complexes, as well as bond angle/distortion and surface charge/pH conditions (Bleam et al., 1989; Kim and Kirkpatrick, 2004). The peaks at 1.8 and −4 ppm can be attributed to Y and P surface precipitates or Y − O − P bonding, according to the reference spectra of Y and P coprecipitation and co-sorption samples (Figs. 5e and 5f, **Text S7**), which also feature dominant peaks at δ_p = -4 ppm, and −10 ppm, along with a shoulder at 1.8 ppm (Figs. 5b - 5d, **Table S1**). The peak centered at −1.5 ppm in reference spectra was not clearly discernible in the sequential sorption spectra, possibly because it overlaps the peak at −4 ppm and shoulder at 1.8 ppm. Additionally, the −10 ppm peak in the sequential sorption spectra can be ascribed to two possible scenarios: i) formation of inner-sphere complexes between P and the kaolinite surface, and/or ii) formation of Y − O − P linkage. However, due to the inherent limitations of 1D ^{31}P NMR and low concentrations of targeted species, distinguishing between these two scenarios by ^{31}P DP/MAS NMR was very challenging. Therefore, further analyses using ^{1}H - ^{31}P CP REAPDOR experiments were employed to characterize the local bonding environments of phosphate, as discussed below.

3.4. *P–Al distances determined by ^{1}H–^{31}P{^{27}Al} CP REAPDOR*

^{1}H–^{31}P{^{27}Al} CP REAPDOR experiment measures ^{31}P–^{27}Al heteronuclear dipolar coupling, which depends strongly on the interatomic distance. This coupling provides key information about P bonding geometries, ligand exchange reactions, and structural configurations on aluminum (hydro)oxide mineral surfaces (Gullion, 1995; Li et al., 2013a). For example, by quantifying the degree of dipolar coupling, the technique enables precise determination of interatomic distances, revealing the spatial arrangement of ^{31}P relative to aluminum (Li et al., 2013a). In this study, the measured interatomic distances provide structural information for phosphate nuclei associated with Al-octahedral layers in kaolinite. Note that, due to the low natural abundance of ^{29}Si and limitation in ^{29}Si NMR data quality, this study only focuses on the interactions among Y, P, and Al-octahedral layers, instead of the Si-tetrahedral layers.

In brief, the REAPDOR experiment consists of a train of rf-pulses applied on the ^{31}P detection channel. These pulses are synchronized with the Magic Angle Spinning (MAS) frequency such that a ^{31}P echo-signal is detected at an evolution time determined by the number of echoes where heteronuclear dipolar couplings are removed (signal S_0). In a second acquisition, an adiabatic recoupling pulse is introduced at the center of the echo-sequence on the ^{27}Al channel. This leads to a re-introduction of the ^{31}P–^{27}Al dipolar coupling, leading to a spectrum with intensity S. Comparing the peak-intensities of with (S) and without recoupling (S_0) allows the calculation of a term $(S_0\text{-}S)/S_0$, which reflects the evolution of the dipolar coupling while the effect of T2-relaxation is eliminated. The value of $(S_0\text{-}S)/S_0$ can be measured as a function of an evolution time (the number of echoes) and it is referred to as REAPDOR fraction. REAPDOR fraction reflects the length of re-coupling period and distance between ^{31}P and ^{27}Al, where a higher value indicates a shorter distance for a given evolution time.

The results revealed that sample 500P (Control I) has the highest REAPDOR fraction at a dephasing time of 1200 μs (Fig. 6d), which indicates the shortest average ^{31}P–^{27}Al distance, as the result of inner-sphere complexation between P and Al-octahedral layers. In contrast, samples 500P500Y, 500Y500P, and 500Y1000P showed slightly lower REAPDOR fractions, which suggest a weaker decoupling between ^{31}P and ^{27}Al and a longer P–Al distances (Fig. 6d). The extended distance after sequential sorption supports our hypothesis of surface interactions between Y and P. REAPDOR results suggest that these interactions increases the separation between P and kaolinite surfaces, potentially through the formation of kaolinite − Y − P surface complexes that prevent direct coordination of phosphate with surface Al. This interpretation is consistent with the increased P/Y uptake in sequential sorption experiments and with the corresponding chemical shifts of Y − O − P bonds observed in 1D ^{31}P NMR spectra.

To further elucidate the molecular structure of the proposed surface complex, detailed analysis of the REAPDOR spectra was performed. Due to the limited data quality even with a long measurement time of over 24 h, clearly distinguishing more than two peaks in the spectra measured for S_0 and S spectra for a specific time remained challenging. Therefore, the data were approximated by fitting the spectra of sequential sorption samples with two peaks at $\delta_p = -4$ ppm (Peak1) and $\delta_p = -10$ ppm (Peak 2), representing two distinct phosphate sites on the kaolinite surface (Fig. 6**a** − **c**). Interestingly, only Peak 2 (P_2, $\delta_p = -10$ ppm) displayed a signal loss from S_0 to S, which suggests a stronger dipolar coupling and a rigid structure between P_2 and surface Al (Fig. 6**a** − **c**). Absolute intensity subtraction between S_0 and S for the sequential sample spectra confirmed the decrease in Peak 2 intensity. This observation, together with −10 ppm resonance observed in 1D ^{31}P NMR spectra, supports the assignment of Peak 2 to an inner-sphere phosphate complex with kaolinite (Fig. 6a). Peak1 (P_1, $\delta_p = -4$ ppm), however, showed very minor intensity change, suggesting that these P environments were located farther from kaolinite surface. In addition, the chemical shift of Peak 1 aligns with that assigned to Y − O − P bonds observed in 1D ^{31}P references spectra (Figs. 5e and 5f), which strongly confirms our hypothesis of Y − O − P bonding formation during sequential sorption. However, the exact coordination environment of these Y-P associated bonding needs further analysis.

3.5. *Numerical simulation of P–Al distances and inference of surface speciation*

To quantify the abovementioned surface structure, the REAPDOR data were compared to SPINEVOLUTION numerical simulation (Veshtort and Griffin, 2006). The simulations generated theoretical REAPDOR fraction curves for 2-spin and 3-spin P/Al clusters, referring to monodentate P − O − Al binding, and bidentate linkage where one P

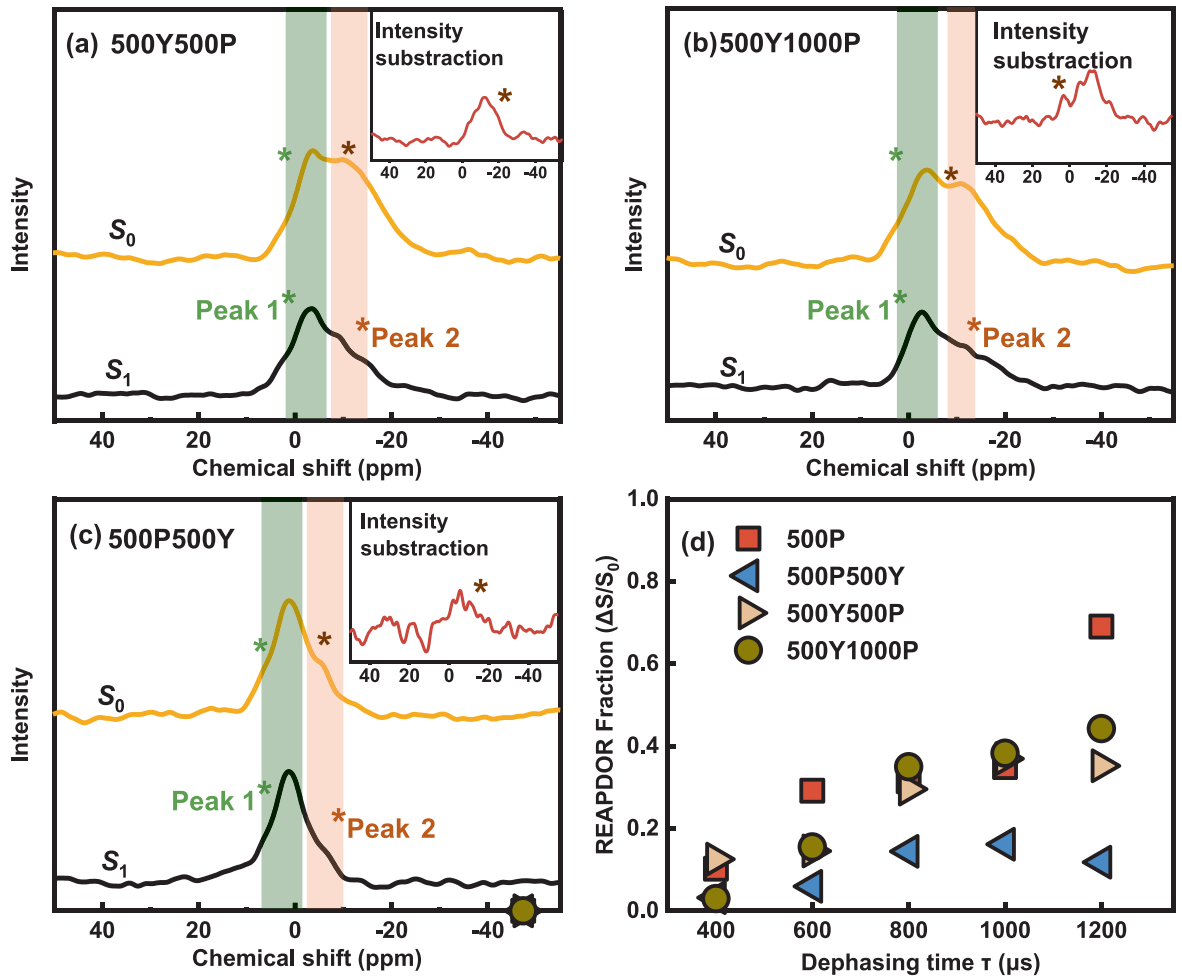

Fig. 6. **(a – c)** Typical set of REAPDOR NMR spectra for S_1 and S_0. Green and orange vertical shadings represent the chemical shift approximately at −4 and −10 ppm, respectively), and **(d)** $^{31}P/^{27}Al$ REAPDOR fraction curve.

site binds to two Al sites, respectively. The simulation considered a series of P – Al distances in a reasonable range and produced a set of REAPDOR fraction curves. The Least squares fit of S and S_0 REAPDOR experimental spectra were performed at Peak 1 (P_1) and Peak 2 (P_2) (Table S2). Integral percentages and distinct REAPDOR fraction curves for P_1 and P_2 were obtained and subsequently fitted to the simulated curves. The correlation coefficient function (corrcoef) was employed in Matlab2022b to evaluate the fitting goodness between experimental and simulated results.

The 2-spin model provided the best fit for the experimental data (Fig. 7), yielding two P – Al distances corresponding to phosphate sites P_1 and P_2. Previous studies have shown that for ion sorption on clay minerals, a distance greater than 4 Å indicates a weak interaction of outer-sphere complex, whereas a shorter distance (less than 4 Å) indicates the formation of more stable inner-sphere complexes (Wu et al., 2023). Hence, 4 Å was used in this study as a threshold to distinguish between inner- and outer- sphere complexes for sorbed P on Al-octahedral layers. Based on the fitting coefficients, the best-fit distances were ~ 5.5 Å for P_1 – Al and 3.8 Å for P_2 – Al scenarios. We therefore propose that, for the longer P_1 – Al distance, – O – Y – bridges between P_1 and Al atoms on kaolinite surfaces, making the observed ~ 5.5 Å distance reasonable. In addition, the P_2 – Al distance of 3.8 Å suggests a P_2 – O – Al surface complex, in which P forms an inner-sphere complex with surface Al-octahedral. This distance is similar to the reported work regarding phosphate sorption on Al (hydro) oxide mineral (Li et al., 2013a). Moreover, simulated REAPDOR curves for the P_2 – O – Al configurations showed a steeper slope than those for the P_1–O–Y···HO-Al scenario, which can be attributed to stronger $^{31}P–^{27}Al$ dipolar coupling, consistent with the shorter P – Al distances (Fig. 7). The 3-spin simulations demonstrated poor goodness-of-fit with the READPDOR experimental data and were consequently excluded from further analysis (Fig. S6). Overall, these results provide strong evidence of surface complexation involving Al-octahedral layers, Y, and P.

3.6. *Morphological evolution*

To further characterize interfacial processes, the morphology and elemental distribution of kaolinite samples were analyzed using HRTEM-EDS. Compared to pure kaolinite samples with clean edges and surfaces (Fig. S7), the sequential sorption samples exhibited a distinctive morphology with flocky edges, indicative of new phase formation (Fig. S8 and S9). While lattice fringes or SAED spots attributable to crystalline Y-phosphates were not observed, we observed rare, patchy domains with Y- and P-enrichment on a few kaolinite particles (Fig. S9); yet we stress that such phases are not commonly occurring in our materials. The images herein are the most direct visual evidence obtainable from TEM, underscoring the need to integrate TEM and NMR for constructing a complete picture of the interfacial reaction mechanisms.

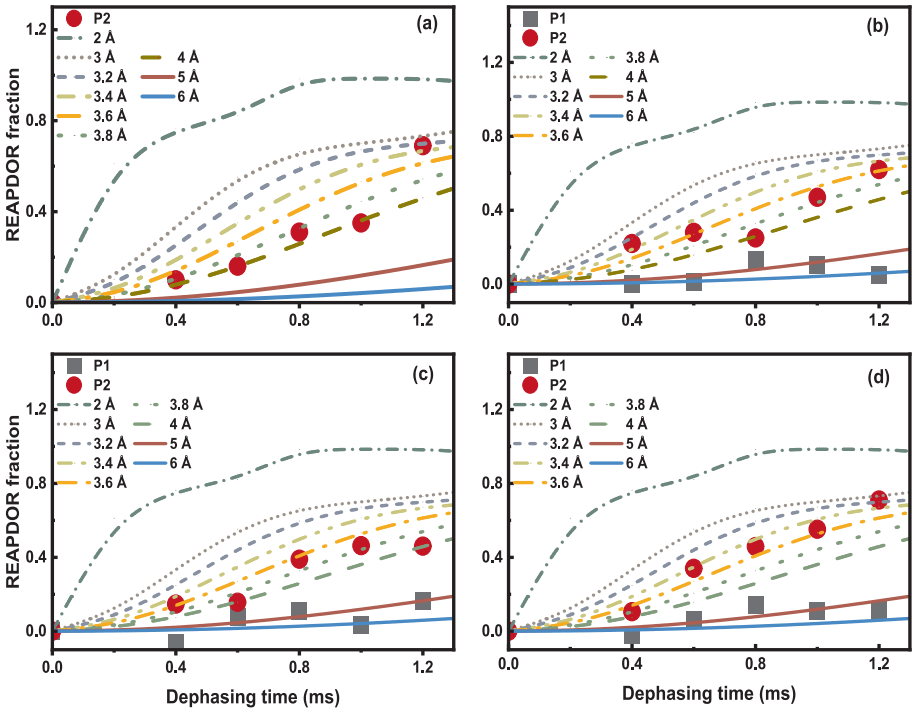

Fig. 7. **(a)** $^{31}P/^{27}Al$ REAPDOR NMR dephasing curves for Peak 1 (P_1, $\delta_p = -4$ ppm) and Peak 2 (P_2, $\delta_p = -10$ ppm) for 500P, **(b)** 500P500Y, **(c)** 500Y500P, and **(d)** 500Y1000P. The SPINEVOLUTION simulations were obtained for 2-spin theoretical models in 3 to 6 Å P–Al distance scenario.

4. Discussion

4.1. Effects of phosphate on REE immobilization and mobilization during chemical weathering

Based on our findings, the proposed reaction mechanism governing Y redistribution influenced by P is illustrated in Fig. 9. Initially, both dissolved Y and P released from primary mineral sources sorb onto the kaolinite surface. Phosphate preferentially forms monodentate inner-sphere complexes with Al-octahedral layers, while Y has been previously reported to form a mixture of outer- and inner-sphere complexes with Al-octahedral and Si-tetrahedral layers (Borst et al., 2020; Fang et al., 2025). Our additional batch sorption experiments at DI water and 10 mM NaCl confirm the coexistence of both outer- and inner-sphere complexes for Y at pH 6, as Y uptake was suppressed at higher ionic strength from ~ 30 % to ~ 20 %, yet a fraction of Y remains strongly bound to the kaolinite surface (**Text S8 and** Fig. 8a).

After this initial uptake, the pre-sorbed species interact with the those in surrounding solution, leading to Y immobilization. Two lines of evidence support this immobilization: first, Y uptake increased when P was pre-sorbed on kaolinite surfaces (vice versa). Even under higher ionic strength, P uptake after Y pre-sorption was slightly higher than that of P sorption-only control (Fig. 8b); and second, 1D ^{31}P MAS NMR detected P-Y association/bonding on kaolinite surfaces. $^{1}H \rightarrow ^{31}P$ CP-REAPDOR further identified this association as a kaolinite – Y – P ternary complex (≡Al – O – Y – O – P) with an Al – P distance of ~ 5.5 Å. We assign this complex primarily to Al-octahedral sites. The reactions at Si-tetrahedral sites cannot be ruled out, but the 7 Å interlayer spacing of kaolinite would place any resulting ^{27}Al–^{31}P distance beyond the ~ 6 Å detection limit of REAPDOR. Further study should consider complementary techniques to gain a more comprehensive understanding.

Interestingly, the sorption sequence of Y and P also influences their surface speciation. The sequential sorption samples (500P500Y, 500Y500P and 500Y1000P) showed similar 1D ^{31}P DP/MAS spectra with minor variations, indicating similar surface phosphate species in all cases. The REAPDOR results, however, revealed a difference: 500P500Y (P sorption first) displayed a flattest dephasing slope compared to samples 500Y500P and 500Y1000P (Y sorption first) (Fig. 6d). Thus, although surface phosphate speciation was generally similar, the average $^{31}P–^{27}Al$ distance was greater when phosphate was pre-sorbed. This likely reflects a shift in the proportion of shorter versus longer $^{31}P–^{27}Al$ distances induced by the occurrence sequence of Y and P.

When Y first sorbed onto kaolinite, it formed a mixture of outer- and inner-sphere complexes with mineral surfaces (Fang et al., 2025). Dissolved P can then react with the sorbed Y in the inner-sphere complex to produce a surface ternary complex. Even at an ionic strength of 10 mM NaCl, the retained Y (Fig. 8a) and the slightly higher P uptake (Fig. 8b) in the sequential sorption compared with control (~6.95 % vs. ~ 6.31 %) confirmed that this proposed pathway still operates. In addition, the pre-sorbed Y complexed with phosphate can further form surface precipitates, as confirmed by TEM (**Fig. S8 and S9**). The calculated saturation index (SI) also shows the thermodynamic likelihood of surface precipitation with respect to $YPO_4{\cdot}nH_2O_{(s)}$ and YPO_4 under the experimental conditions (Table 2).

Reversing the occurrence sequence (P first followed by Y addition) reveals a similar mechanism with slight differences in the proportions of surface complexes and precipitates. REAPDOR results for 500P500Y exhibit the flattest dephasing curve, indicating a longer average Al–P distance, likely due to higher proportion of surface precipitates (Figs. 9d and 9e). According to sorption uptake and MINTEQ modeling, ~50 μM sorbed P on kaolinite surfaces in the Step 1 of 500P500Y interacted with dissolved Y, whereas only ~ 13 μM sorbed Y in the Step 1 of 500Y500P and 500Y1000P was available. Since a solution containing ~ 10 μM dissolved Y and P is supersaturated with respect to $YPO_4{\cdot}nH_2O$ (Table 2), the higher surface bound P thermodynamically favors surface precipitation in the P-first sequence. A smaller fraction of ternary complexes (≡Al – O – Y – O – P) may also form, as indicated by REAPDOR simulations. One possible reaction was ligand exchange between Y and the initially sorbed P within inner-sphere complex.

In summary, our findings provide a fundamental understanding of how P as a natural ligand governs Y behaviors during redistribution. Because Y shares similar electronic configurations and geochemical

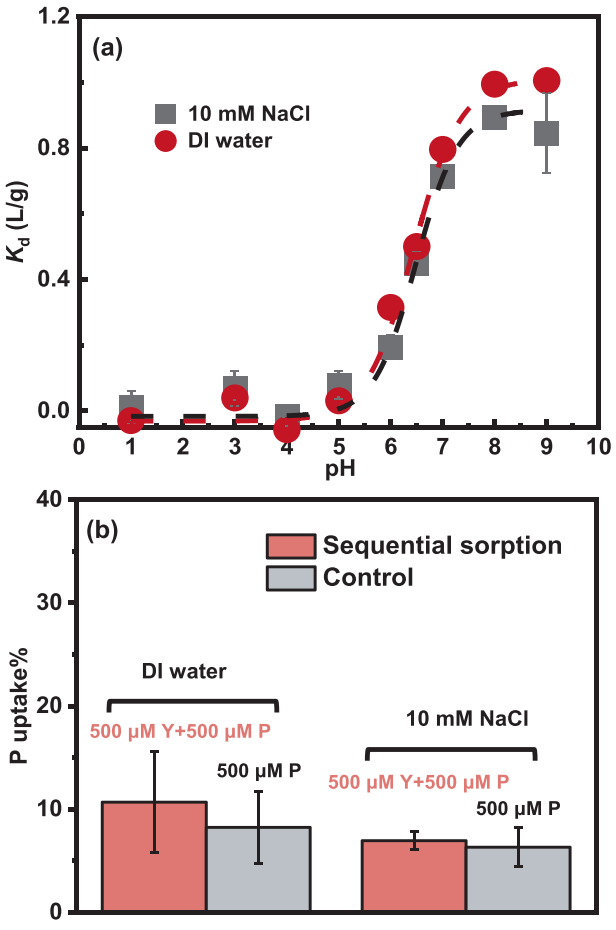

Fig. 8. The distribution coefficient ($K_d = C_0$-C_{eq}/C_{eq}, C_0: initial concentration; C_t: the species concentration at sorption equilibrium) with 50 μM initial concentration of dissolved Y in DI water and 10 mM NaCl at pH 1–9 (a); the phosphate uptake of sequential sorption and control under DI water (left) and 10 mM NaCl (right) at pH 6.0 ± 2.0.

patterns with other heavy REEs, these results can be generally extended to the heavy REE group. Phosphate lowers Y mobility by forming kaolinite − Y − O − P surface complex and Y-P surface precipitate. The relative importance of these two pathways depends on the order in which Y and P encounter the clay surface, their respective surface affinities, and the saturation conditions. Aging is also likely to further modify the surface structures. After one-month aging, the 500Y500P sample showed an increased integrated proportion at −4 ppm (representing Y-P associations) and a decreased −10 ppm peak (representing P sorption only species) (**Text S8 and Fig. S10**). These shift suggests that, over longer timescales, these surface complexes and precipitates may reorganized into well-ordered secondary REE-phosphate minerals such as rhabdophane, florencite, and overgrowth xenotime in natural environments (Bern et al., 2016).

4.2. Methodological implications for studying REE behaviors in complex natural matrix

The study demonstrates that solid-state NMR spectroscopy is an effective approach for characterizing REE coordination in clay-REE-ligand systems. Characterization techniques such as Fourier-transform infrared spectroscopy (FTIR), X-ray fluorescence spectroscopy (XRF), and X-ray absorption spectroscopy (XAS) often face limitations including spectral overlap, limited sensitivity, low data quality at trace concentrations, and uncertainties in shell-by-shell fitting for REE coordination (Dutta, 2017; Grünert and Klementiev, 2020; Kerisit and Prange, 2019; Schramm, 2016; Smith, 2011). XAS is a particularly powerful techniques which can reveal the oxidation states, local coordination environments, and electronic structures of REE in different matrices (Henderson et al., 2014; Koningsberger and Prins, 1987). However, it can be challenging to discern subtle changes in REE coordination due to the data quality and inherent spectral similarities (Liu et al., 2019). Such challenges are amplified in REE-clay systems, where local bonding is complex and the adsorption mechanisms that drive REE enrichment and fractionation in regolith-hosted deposits remain debated (Fang et al., 2025; Sanematsu and Watanabe, 2016). Our Y K-edge EXAFS results demonstrated these limitations: the spectra for Y-only sorption, Y-P sequential sorption, and bulk Y-P precipitation are nearly identical and the poor quality of *k*-space oscillation made further structural analysis inconclusive (**Fig. S4**). Yet, a molecular-scale understanding of REE behavior is critical for explaining their occurrence, transport, and redistribution in highly-weathered natural reserves, which serves as an important commercial source of REE resources.

In contrast to the spectroscopic techniques discussed above, the solid-state NMR applied in this study targets NMR-sensitive nuclei (e.g., ^{13}C, ^{27}Al, and ^{31}P), which allows interatomic distances to be inferred and REE interactions with mineral surfaces and natural ligands to be characterized. $^{1}H-^{31}P\{^{27}Al\}$ CP REAPDOR NMR spectroscopy, especially coupled with numerical simulations of dipolar coupling effects, enables quantification of atomic distance between redeposited REE and kaolinite surfaces, thereby revealing interfacial reaction mechanisms. Utilizing REAPDOR with numerical fitting to distinguish monodentate inner-sphere vs. Y-bridged ternary complexes is rarely reported in REE-mineral studies and thus represents methodological progress. Despite its strengths, this NMR-based approach also has limitations: it is model-dependent and time-consuming. The numerical simulation and data interpretation rely on certain assumptions and predefined models, as demonstrated by our use of 2- and 3-spin scenarios. Additionally, each sample requires 24 h of data collection due to the low concentration of targeted nuclei. Nevertheless, elucidating REE speciation and local structures during geochemical processes is inherently challenging and necessitates the integration of multiple complementary techniques.

4.3. Implications for the prediction, recovery, and understanding of REE occurrences

Naturally occurring inorganic ligands such as phosphate play a significant role in the transport and redistribution of REE during weathering. Depending on geochemical conditions, ligand complexation reactions can either enhance REE solubility/mobility or induce REE precipitation/immobilization on mineral surfaces or in bulk solution. These processes heavily influence REE distribution and associated biogeochemical cycling in natural weathered deposits. Our results provide evidence that phosphate can effectively immobilize Y by forming surface ternary complexes and surface precipitates. We also elucidated the surface molecular structure of such complexes. Since Y has similar ionic radius and coordination structure as other heavy REEs (Dy–Lu), which have shown to display comparable environmental behaviors, e.g., sorption capacities on clay minerals and comparable distribution patterns in various geological setting (Yang et al., 2019; Zaharescu et al., 2017), our findings can be reasonably extrapolated to the heavy REE group. Such extrapolation helps explain the widespread occurrences and speciation of REE-phosphate minerals in natural reserves, particularly in weathered sedimentary environments.

Additionally, understanding ligand-mediated interactions is essential for predicting REE distributions in weathering systems and for assessing resource potential. From a resource recovery perspective, the molecular-scale bonding environment of REE and resulting macro-scale mineralogy determine extraction efficiency. For example, ion exchange methods (e.g., ammonium sulfate leaching) have been commonly applied to extract REE from IADs, where REE is weakly bound to clay minerals. However, the effectiveness of ion exchange methods may be

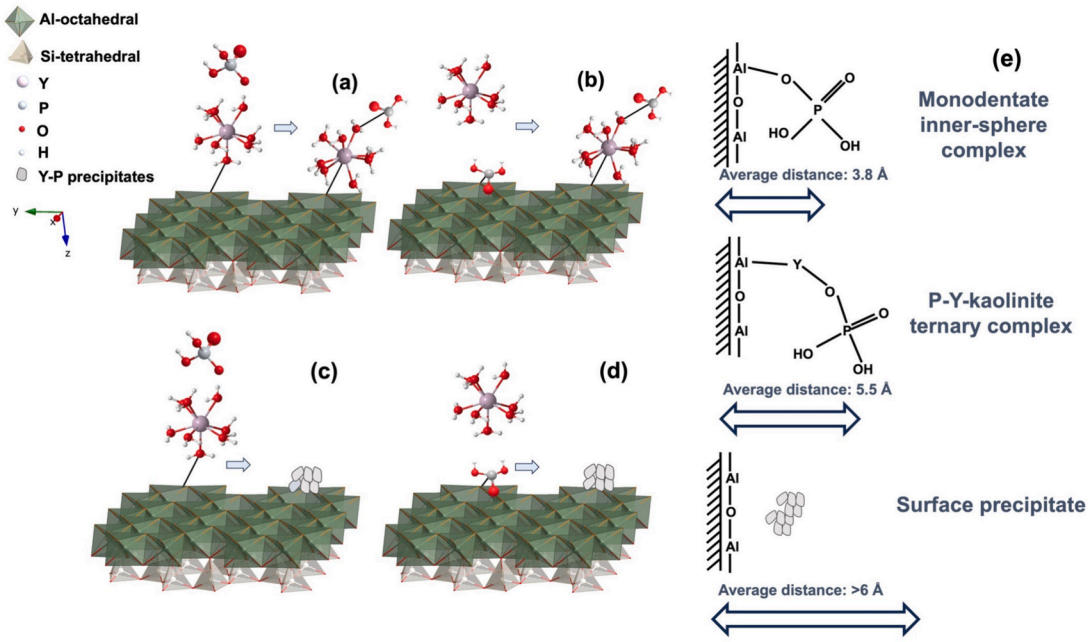

Fig. 9. Schematic of the proposed reaction mechanism during sequential sorption on kaolinite surfaces. **(a-b)** formation of kaolinite − Y − P surface ternary complex. **(c-d)** formation of Y − P surface precipitates. **(e)** The surface molecular structure.

Table 2
Saturation Indices (SI) with respect to $YPO_4{\cdot}nH_2O_{(s)}$ and YPO_4 at pH 6 calculated by PHREEQC.

Y concentration (μM)	P concentration (μM)	SI ($YPO_4{\cdot}nH_2O_{(s)}$)	SI ($YPO_{4(s)}$)
10	10	6.068	6.888
10	500	6.419	7.239
20	50	6.468	7.288
50	50	6.958	7.778
100	100	7.306	8.126
200	200	7.640	8.460
500	50	7.117	7.937
500	500	8.068	8.888

limited for REE-P-clay mineral complexes or REE-bearing minerals with high weathering resistance such as monazite or xenotime (Moldoveanu and Papangelakis, 2013). Therefore, it is critical to assess the extraction and recovery strategies, and their economic feasibility, for different types of REE resources.

Based on our findings, several important perspectives warrant further investigation. First, while this study primarily focuses on the redistribution of dissolved Y and P, it does not address the mineral dissolution processes that initiate REE release. Previous studies suggest that REE profiles in secondary deposits are heavily influenced by primary mineral inheritances with varied weathering resistance (Boxleiter and Elliott, 2023). Chemically less stable REE-bearing minerals, such as bastnasite, synchysite-(Ce/Y), allanite, and titanite, as well as phosphate accessory minerals (e.g., apatite, fluorapatite), tend to decompose during early weathering stages and release REE or ligands into weathering crust (Banfield and Eggleton, 1989; Sanematsu et al., 2016). However, the subsequent transformation and redistribution are still poorly understood due to the complexity of natural matrix. Additionally, biotic factors, including fungal hyphae and bacteria that secrete extracellular polymeric substances, also promote mineral dissolution (He et al., 2023; Taunton et al., 2000). Understanding the interplay of microbial and geochemical constraints on REE release, transport and redistribution requires further study. Finally, differences in complex stability, mobility, enrichment, and fractionation of HREE vs. LREE may lead to distinct patterns of secondary REE-bearing phases. The underlying reaction mechanisms responsible for these variations also warrant further investigations to enhance the understanding of REE behaviors in natural settings.

5. Conclusion

This study investigated the effects of phosphate on Y sorption by kaolinite. The results showed that phosphate reduced Y mobility by Y-P complexation and heterogeneous precipitation on kaolinite surfaces. Two distinct phosphate surface species were identified during sequential sorption. $^{1}H-^{31}P$ CP REAPDOR NMR analysis and numerical simulation further revealed that these two surface species correspond to i) adsorbed phosphate on Al-octahedral layers through monodentate inner-sphere complexation, with an average P−Al distance of 3.8 Å; and ii) kaolinite−Y−P ternary surface complexes, with an average P−Al distance of 5.5 Å. These findings provide direct molecular-scale evidence for the formation and occurrence of REE-phosphate minerals and advance our understanding of REE interactions with natural ligands at the mineral–water interface. More broadly, the findings highlight the critical role of competitive adsorption and surface complexation on kaolinite, especially in highly weathered environments. Overall, this study offers valuable insight into the fundamental reaction mechanisms controlling REE immobilization, mobilization, transport, and redeposition in natural REE resources settings.

Data availability

Data are available through Mendeley Data at: https://doi.org/10.17632/44v9fm7y2r.1.

CRediT authorship contribution statement

Hang Xu: Writing – review & editing, Writing – original draft, Visualization, Validation, Methodology, Investigation, Formal analysis, Data curation. **Johannes Leisen:** Writing – review & editing, Methodology, Investigation, Formal analysis. **Alicia S. Robang:** Writing – review & editing, Investigation, Formal analysis, Data curation. **Yinghao Wen:** Writing – review & editing, Investigation. **Biao Wan:** Writing – review & editing, Investigation. **Simin Zhao:** Writing – review &

editing, Investigation. **Anant Paravastu:** Writing – review & editing, Supervision, Investigation. **Brian L. Phillips:** Writing – review & editing, Supervision, Formal analysis. **Yuanzhi Tang:** Writing – review & editing, Supervision, Resources, Project administration, Methodology, Funding acquisition, Conceptualization.

Declaration of competing interest

The authors declare that they have no known competing financial interests or personal relationships that could have appeared to influence the work reported in this paper.

Acknowledgement

This work was supported by the NSF Grant #2327660. A portion of the measurements were conducted at the Georgia Tech Institute for Matter and Systems, a member of the National Nanotechnology Coordinated Infrastructure (NNCI), which is supported by the National Science Foundation (Grant ECCS-2025462). The authors acknowledge beamline scientists at the Advanced Photon Source (APS) for help with data collection. The authors acknowledge Yixuan Yang for assistance with TEM data processing.

Appendix A. Supplementary material

Supplementary materials contain: **Text:** Y and P sorption on kaolinite: pH edge experiments (**Text S1**), isotherm experiments at pH 6 (**Text S2**); Inductively coupled plasma – mass spectroscopy (ICP-MS) analysis (**Text S3**); Thermodynamic modeling using PHREEQC and MINTEQ (**Text S4**); ^{31}P DP/MAS solid-state NMR measurements (**Text S5**); ^{1}H– ^{31}P CP REAPDOR solid-state NMR spectroscopy and SPINEVOLUTION numerical simulation (**Text S6**); Coprecipitation and cosorption of yttrium and phosphate (**Text S7**); Additional batch sorption experiments (**Text S8**). **Tables:** Deconvolution and Gaussian fitting analysis of different phosphate species for 1 D solid-state ^{31}P NMR spectra (Table S1); Decompostion of REAPDOR experimental spectra (S and S_0) of sequential sorption samples at Peak1 (P_1, δp = -4 ppm) and Peak 2 (P_2, δp = -10 ppm(Table S2). **Figures:** The recovery of phosphate and yttrium during washing processes in sequential sorption experiments (Fig. S1); Y sorption isotherm on kaolinite at pH 6 (Fig. S2); Phosphate sorption isotherm on kaolinite at pH 6 (Fig. S3); k^2-weighted Y K-edge EXAFS data (Fig. S4); Least-squares fits of 1D ^{31}P solid-state NMR spectra of sequential sorption samples, Y and P coprecipitation sample, and Y and P cosorption sample (Fig. S5); ^{1}H– ^{31}P CP REAPDOR NMR dephasing curves for Ads-500P, Seq-500P-500Y, Seq-500Y-500P, and Seq-500Y-1000P (3-spin theoretical model) (Fig. S6); High resolution transmission electron microscopy (HRTEM) images and selected area electron diffraction (SAED) of pristine kaolinite sample (Fig. S7); HRTEM images and HRTEM-EDS layered images, and EDS spectra of seq-500Y-500P, seq-500Y-1000P, and seq-500P-500Y (Fig. S8); HRTEM images for searching of the potential Y-P precipitates at kaolinite surfaces (Fig. S9); The least-squares fits of 1D ^{31}P solid-state NMR spectra for Seq-500Y-500P after overnight and one-month aging (Fig. S10). Supplementary material to this article can be found online at https://doi.org/10.1016/j.gca.2025.09.040.

References

Aubert, D., Stille, P., Probst, A., 2001. REE fractionation during granite weathering and removal by waters and suspended loads: Sr and Nd isotopic evidence. Geochim. Cosmochim. Acta 65 (3), 387–406.
Banfield, J.F., Eggleton, R.A., 1989. Apatite replacement and rare earth mobilization, fractionation, and fixation during weathering. Clay Clay Miner. 37, 113–127.
Bern, C.R., Shah, A.K., Benzel, W.M., Lowers, H.A., 2016. The distribution and composition of REE-bearing minerals in placers of the Atlantic and Gulf coastal plains, USA. J. Geochem. Explor. 162, 50–61.
Bleam, W.F., Pfeffer, P.E., Frye, J.S., 1989. 31P solid-state nuclear magnetic resonance spectroscopy of aluminum phosphate minerals. Phys. Chem. Miner. 16 (5), 455–464.
Borst, A.M., Smith, M.P., Finch, A.A., Estrade, G., Villanova-de-Benavent, C., Nason, P., Marquis, E., Horsburgh, N.J., Goodenough, K.M., Xu, C., 2020. Adsorption of rare earth elements in regolith-hosted clay deposits. Nat. Commun. 11 (1), 4386.
Boxleiter, A., Elliott, W.C., 2023. Rare-earth minerals in kaolin ore, mine tailings, and sands–central georgia, upper coastal plain. Clay Clay Miner. 71 (3), 274–308.
Byrne, R.H., Liu, X., Schijf, J., 1996. The influence of phosphate coprecipitation on rare earth distributions in natural waters. Geochim. Cosmochim. Acta 60 (17), 3341–3346.
Cade-Menun, B.J., 2005. Characterizing phosphorus in environmental and agricultural samples by ^{31}P nuclear magnetic resonance spectroscopy. Talanta 66 (2), 359–371.
Cheshire, M.C., Bish, D.L., Cahill, J.F., Kertesz, V., Stack, A.G., 2018. Geochemical evidence for rare-earth element mobilization during kaolin diagenesis. ACS Earth Space Chem. 2 (5), 506–520.
Costa, N.O., Botelho, N.F., Garnier, J., 2020. Concentration of rare earth elements in the Faixa Placha tin deposit, Pedra Branca A-Type Granitic Massif, central Brazil, and its potential for ion-adsorption-type REE-Y mineralization. Ore Geol. Rev. 123, 103606.
Ding, Y., Chen, Y., Pradel, K.C., Zhang, W., Liu, M., Wang, Z.L., 2018. Domain structures and Prco antisite point defects in double-perovskite $PrBaCo_2O^{5+}$ and $PrBa_{0.8}Ca_{0.2}Co_2O^{5+}$. Ultramicroscopy 193, 64–70.
Dushyantha, N., Batapola, N., Ilankoon, I., Rohitha, S., Premasiri, R., Abeysinghe, B., Ratnayake, N., Dissanayake, K., 2020. The story of rare earth elements (REEs): Occurrences, global distribution, genesis, geology, mineralogy and global production. Ore Geol. Rev. 122, 103521.
Dutta, A., 2017. Fourier transform infrared spectroscopy. *Spectroscopic methods for nanomaterials characterization* pp: 73 - 93.
Elliott, W.C., 2020. Regolith-hosted rare-earth elements: the phyllosilicate connection. Am. Mineral. 105 (1), 1–2.
Elliott, W.C., Gardner, D.J., Malla, P., Riley, E., 2018. A new look at the occurrences of the rare-earth elements in the Georgia kaolins. Clay Clay Miner. 66 (3), 245–260.
Emsbo, P., McLaughlin, P.I., Breit, G.N., du Bray, E.A., Koenig, A.E., 2015. Rare earth elements in sedimentary phosphate deposits: solution to the global REE crisis? Gondw. Res. 27 (2), 776–785.
Fang, Y., Lee, S.S., Ledingham, G.J., Stubbs, J.E., Eng, P.J., Catalano, J.G., 2025. Complex adsorption behavior of neodymium and ytterbium on structurally-distinct alumina surfaces. Environ. Sci. & Technolog 59 (8), 3972–3981.
Feng, X., Onel, O., Council-Troche, M., Noble, A., Yoon, R.-H., Morris, J.R., 2021. A study of rare earth ion-adsorption clays: the speciation of rare earth elements on kaolinite at basic pH. Appl. Clay Sci. 201, 105920.
Föllmi, K., 1996. The phosphorus cycle, phosphogenesis and marine phosphate-rich deposits. Earth Sci. Rev. 40 (1–2), 55–124.
Fu, X., Yi, Z., Fu, W., Liu, J., Han, Z., Fang, G., Sha, X., Liu, X., Xu, C., 2024. Mineralogy and weathering of REE minerals in the Liuchen granite, Guangxi, southern China: Implications for HREE enrichment in the granite regolith. Ore Geol. Rev. 169, 106099.
Ganor, J., Cama, J., Metz, V., 2003. Surface protonation data of kaolinite—re-evaluation based on dissolution experiments. J. Colloid Interface Sci. 264 (1), 67–75.
Giovannini, A.L., Neto, A.C.B., Porto, C.G., Pereira, V.P., Takehara, L., Barbanson, L., Bastos, P.H., 2017. Mineralogy and geochemistry of laterites from the Morro dos Seis Lagos Nb (Ti, REE) deposit (Amazonas, Brazil). Ore Geol. Rev. 88, 461–480.
Goodenough, K.M., Wall, F., Merriman, D., 2018. The rare earth elements: demand, global resources, and challenges for resourcing future generations. Nat. Resour. Res. 27, 201–216.
Grünert, W., Klementiev, K., 2020. X-ray absorption spectroscopy principles and practical use in materials analysis. Phys. Sci. Rev. 5 (4), 20170181.
Gullion, T., 1995. Measurement of dipolar interactions between spin-12 and quadrupolar nuclei by rotational-echo, adiabatic-passage, double-resonance NMR. Chem. Phys. Lett. 246 (3), 325–330.
He, Y., Ma, L., Li, X., Wang, H., Liang, X., Zhu, J., He, H., 2023. Mobilization and fractionation of rare earth elements during experimental bio-weathering of granites. Geochim. Cosmochim. Acta 343, 384–395.
Henderson, G.S., De Groot, F.M., Moulton, B.J., 2014. X-ray absorption near-edge structure (XANES) spectroscopy. Rev. Mineral. Geochem. 78 (1), 75–138.
Huang, J., Tan, W., Liang, X., He, H., Ma, L., Bao, Z., Zhu, J., 2021a. REE fractionation controlled by REE speciation during formation of the Renju regolith-hosted REE deposits in Guangdong Province, South China. Ore Geol. Rev. 134, 104172.
Huang, Y., He, H., Liang, X., Bao, Z., Tan, W., Ma, L., Zhu, J., Huang, J., Wang, H., 2021b. Characteristics and genesis of ion adsorption type REE deposits in the weathering crusts of metamorphic rocks in Ningdu, Ganzhou, China. Ore Geol. Rev. 135, 104173.
Janots, E., Bernier, F., Brunet, F., Muñoz, M., Trcera, N., Berger, A., Lanson, M., 2015. Ce (III) and Ce(IV) (re)distribution and fractionation in a laterite profile from Madagascar: Insights from in situ XANES spectroscopy at the Ce L_{III}-edge. Geochim. Cosmochim. Acta 153, 134–148.
Jonasson, R., Bancroft, G., Nesbitt, H., 1985. Solubilities of some hydrous REE phosphates with implications for diagenesis and sea water concentrations. Geochim. Cosmochim. Acta 49 (10), 2133–2139.
Kanazawa, Y., Kamitani, M., 2006. Rare earth minerals and resources in the world. J. Alloy. Compd. 408, 1339–1343.
Kerisit, S.N., Prange, M.P., 2019. Ab initio molecular dynamics simulation of divalent metal cation incorporation in calcite: implications for interpreting X-ray absorption spectroscopy data. ACS Earth Space Chem. 3 (11), 2582–2592.
Kim, Y., Kirkpatrick, R., 2004. An investigation of phosphate adsorbed on aluminium oxyhydroxide and oxide phases by nuclear magnetic resonance. Eur. J. Soil Sci. 55 (2), 243–251.

Koningsberger, D.C., Prins, R., 1987. X-ray absorption: principles, applications, techniques of EXAFS, SEXAFS and XANES. *John Wiley & Sons*, New York. ISBN: 978 - 0 - 471 - 87547 - 5.
Lee, J.H., Byrne, R.H., 1993. Complexation of trivalent rare earth elements (Ce, Eu, Gd, Tb, Yb) by carbonate ions. Geochim. Cosmochim. Acta 57 (2), 295–302.
Li, M.Y.H., Zhou, M.-F., 2020. The role of clay minerals in formation of the regolith-hosted heavy rare earth element deposits. Am. Mineral. 105 (1), 92–108.
Li, M.Y.H., Zhou, M.-F., Williams-Jones, A.E., 2019. The genesis of regolith-hosted heavy rare earth element deposits: Insights from the world-class Zudong deposit in Jiangxi Province, South China. Econ. Geol. 114 (3), 541–568.
Li, W., Feng, X., Yan, Y., Sparks, D.L., Phillips, B.L., 2013a. Solid-state NMR spectroscopic study of phosphate sorption mechanisms on aluminum (hydr) oxides. Environ. Sci. Technol. 47 (15), 8308–8315.
Li, W., Pierre-Louis, A.-M., Kwon, K.D., Kubicki, J.D., Strongin, D.R., Phillips, B.L., 2013b. Molecular level investigations of phosphate sorption on corundum (α-Al_2O_3) by ^{31}P solid state NMR, ATR-FTIR and quantum chemical calculation. Geochim. Cosmochim. Acta 107, 252–266.
Li, Z., Schulz, L., Ackley, C., Fenske, N., 2010. Adsorption of tetracycline on kaolinite with pH-dependent surface charges. J. Colloid Interface Sci. 351 (1), 254–260.
Liu, P., Huang, R., Tang, Y., 2019. Comprehensive understandings of rare earth element (REE) speciation in coal fly ashes and implication for REE extractability. Environ. Sci. Technol. 53 (9), 5369–5377.
Liu, X., Byrne, R.H., 1997. Rare earth and yttrium phosphate solubilities in aqueous solution. Geochim. Cosmochim. Acta 61 (8), 1625–1633.
Liu, X., Tournassat, C., Grangeon, S., Kalinichev, A.G., Takahashi, Y., Marques Fernandes, M., 2022. Molecular-level understanding of metal ion retention in clay-rich materials. Nat. Rev. Earth & Environ. 3 (7), 461–476.
Louvel, M., Etschmann, B., Guan, Q., Testemale, D., Brugger, J., 2022. Carbonate complexation enhances hydrothermal transport of rare earth elements in alkaline fluids. Nat. Commun. 13 (1), 1456.
Moldoveanu, G.A., Papangelakis, V.G., 2013. Recovery of rare earth elements adsorbed on clay minerals: II. Leaching with ammonium sulfate. Hydrometallurgy 131–132, 158–166.
Murphy, J., Riley, J.P., 1962. A modified single solution method for the determination of phosphate in natural waters. Anal. Chim. Acta 27, 31–36.
Ormerod, J., Karati, A., Baghel, A.P.S., Prodius, D., Nlebedim, I.C., 2023. Sourcing, refining and recycling of rare-earth magnets. Sustainability 15 (20), 14901.
Parkhurst, D.L., Appelo, C., 2013. Description of input and examples for PHREEQC version 3—a computer program for speciation, batch-reaction, one-dimensional transport, and inverse geochemical calculations. US geological survey techniques and methods, Book 6, Chapter A43, 497p.
Ramazanova, E., Sharma, N., Flynn, E.D., Stagg, O., Catalano, J.G., Giammar, D.E., 2025. Adsorption of REEs to kaolinite via ion exchange and surface complexation as a function of water chemistry. ACS Earth Space Chem. 9 (6), 1430–1442.
Sanematsu, K., Ejima, T., Kon, Y., Manaka, T., Zaw, K., Morita, S., Seo, Y., 2016. Fractionation of rare-earth elements during magmatic differentiation and weathering of calc-alkaline granites in southern Myanmar. Mineral. Mag. 80 (1), 77–102.
Sanematsu, K., Watanabe, Y., 2016. Characteristics and genesis of ion adsorption-type rare earth element deposits. Rev. Econ. Geol. 18, 55–79.
Schoonheydt, R.A., Johnston, C.T., 2013. Chapter 5 - surface and interface chemistry of clay minerals. In: Bergaya, F., Lagaly, G. (Eds.), Developments in Clay Science. Elsevier, pp. 139–172.
Schramm, R., 2016. Use of X-ray fluorescence analysis for the determination of rare earth elements. Phys. Sci. Rev. 1 (9), 20160061.
Schroth, B.K., Sposito, G., 1997. Surface charge properties of kaolinite. Clay Clay Miner. 45, 85–91.
Smith, B.C., 2011. Fundamentals of Fourier transform infrared spectroscopy. CRC Press, Boca Rton.
Stolpe, B., Guo, L., Shiller, A.M., 2013. Binding and transport of rare earth elements by organic and iron-rich nanocolloids in Alaskan rivers, as revealed by field-flow fractionation and ICP-MS. Geochim. Cosmochim. Acta 106, 446–462.
Tang, J., Johannesson, K.H., 2010. Ligand extraction of rare earth elements from aquifer sediments: Implications for rare earth element complexation with organic matter in natural waters. Geochim. Cosmochim. Acta 74 (23), 6690–6705.
Taunton, A.E., Welch, S.A., Banfield, J.F., 2000. Microbial controls on phosphate and lanthanide distributions during granite weathering and soil formation. Chem. Geol. 169 (3), 371–382.
Turner, D.J., 2015. Reflectance spectroscopy and imaging spectroscopy of rare earth element-bearing mineral and rock samples. University of British Columbia, Vancouver, BC, Canada.
Veshtort, M., Griffin, R.G., 2006. SPINEVOLUTION: a powerful tool for the simulation of solid and liquid state NMR experiments. J. Magn. Reson. 178 (2), 248–282.
Wang, G., Xu, J., Ran, L., Zhu, R., Ling, B., Liang, X., Kang, S., Wang, Y., Wei, J., Ma, L., 2023a. A green and efficient technology to recover rare earth elements from weathering crusts. Nat. Sustainability 6 (1), 81–92.
Wang, Y., Liu, L., Sun, M., Huang, J., Huang, Y., Liang, X., Tan, W., He, H., Zhu, J., 2023b. Distribution and fractionation of rare earth elements (REE) in the ion adsorption-type REE deposit (IAD) at Maofeng Mountain, Guangzhou, China. Clays and Clay Minerals 71 (3), 340–361.
Wu, Z., Chen, Y., Wang, Y., Xu, Y., Lin, Z., Liang, X., Cheng, H., 2023. Review of rare earth element (REE) adsorption on and desorption from clay minerals: Application to formation and mining of ion-adsorption REE deposits. Ore Geol. Rev. 105446.
Xu, C., Kynický, J., Smith, M.P., Kopriva, A., Brtnický, M., Urubek, T., Yang, Y., Zhao, Z., He, C., Song, W., 2017. Origin of heavy rare earth mineralization in South China. Nat. Commun. 8 (1), 14598.
Xu, Y., Luo, C., Gao, L., Long, J., Xu, H., Yang, R., 2022. Anomalous concentrations and environmental implications of rare earth elements in the rock-soil-moss system in the black shale area. Chemosphere 307, 135770.
Yan, Y., Koopal, L.K., Li, W., Zheng, A., Yang, J., Liu, F., Feng, X., 2015. Size-dependent sorption of myo-inositol hexakisphosphate and orthophosphate on nano-γ-Al_2O_3. J. Colloid Interface Sci. 451, 85–92.
Yang, L., Steefel, C.I., 2008. Kaolinite dissolution and precipitation kinetics at 22 C and pH 4. Geochim. Cosmochim. Acta 72 (1), 99–116.
Yang, M., Liang, X., Ma, L., Huang, J., He, H., Zhu, J., 2019. Adsorption of REEs on kaolinite and halloysite: a link to the REE distribution on clays in the weathering crust of granite. Chem. Geol. 525, 210–217.
Zaharescu, D.G., Burghelea, C.I., Dontsova, K., Presler, J.K., Maier, R.M., Huxman, T., Domanik, K.J., Hunt, E.A., Amistadi, M.K., Gaddis, E.E., 2017. Ecosystem composition controls the fate of rare earth elements during incipient soil genesis. Sci. Rep. 7 (1), 43208.
Zhang, N., Yan, H., Li, L., Wu, R., Song, L., Zhang, G., Liang, W., He, H., 2021. Use of rare earth elements in single-atom site catalysis: a critical review—Commemorating the 100th anniversary of the birth of Academician Guangxian Xu. J. Rare Earths 39 (3), 233–242.
Zhou, X., Ning, L., Qiao, J., Zhao, Y., Xiong, P., Xia, Z., 2022. Interplay of defect levels and rare earth emission centers in multimode luminescent phosphors. Nat. Commun. 13 (1), 7589.